



Identifying the Origins of Microstructural Defects Such as Cracking within Ni-Rich NMC811 Cathode Particles for Lithium-Ion Batteries

Thomas M. M. Heenan, Aaron Wade, Chun Tan, Julia E. Parker, Dorota Matras, Andrew S. Leach, James B. Robinson, Alice Llewellyn, Alexander Dimitrijevic, Rhodri Jervis, Paul D. Quinn, Dan J. L. Brett, and Paul R. Shearing*

The next generation of automotive lithium-ion batteries may employ NMC811 materials; however, defective particles are of significant interest due to their links to performance loss. Here, it is demonstrated that even before operation, on average, one-third of NMC811 particles experience some form of defect, increasing in severity near the separator interface. It is determined that defective particles can be detected and quantified using low resolution imaging, presenting a significant improvement for material statistics. Fluorescence and diffraction data reveal that the variation of Mn content within the NMC particles may correlate to crystallographic disordering, indicating that the mobility and dissolution of Mn may be a key aspect of degradation during initial cycling. This, however, does not appear to correlate with the severity of particle cracking, which when analyzed at high spatial resolutions, reveals cracking structures similar to lower Ni content NMC, suggesting that the disconnection and separation of neighboring primary particles may be due to electrochemical expansion/contraction, exacerbated by other factors such as grain orientation that are inherent in such polycrystalline materials. These findings can guide research directions toward mitigating degradation at each respective length-scale: electrode sheets, secondary and primary particles, and individual crystals, ultimately leading to improved automotive ranges and lifetimes.

durable to fast-charging and capable of high capacities for long-range operation are required. BEV range is largely limited by the individual lithium-ion (Li-ion) cell energies, which in turn is dictated by the electrode chemistry and operating conditions, for example: the choice of anode and cathode, charging rate, and upper cut-off voltage. In commercial applications, the anode is often sized in accordance to the achievable capacity of the cathode, plus an appropriate safety buffer, and consequently, in many situations, the cathode dictates the cell capacity, and thus BEV range,^[1] and the cell is said to be “cathode limited.”

A variety of layered transition metal oxide materials have been developed to operate as the cathode for Li-ion cells. For instance, the discovery of LiCoO₂ (LCO) in 1980 revolutionized the portable electronics industry;^[2] however, because the Co^{3+/4+} energy band overlaps with the O²⁻, LCO suffers low practical capacities due to instabilities at higher voltages that can trigger oxygen release.^[3] Consequently,

the Co can be substituted with Ni or Mn, which possess better chemical stabilities, to produce LiNiO₂ or LiMn₂O₄.^[4,5] Alas, Ni and Mn have lower structural stabilities than Co and consequently, the former can result in poor thermal stability and

1. Introduction

For battery electric vehicles (BEVs) to become truly competitive within the automotive market, affordable batteries that are

Dr. T. M. M. Heenan, A. Wade, Dr. C. Tan, Dr. A. S. Leach, Dr. J. B. Robinson, A. Llewellyn, A. Dimitrijevic, Dr. R. Jervis, Prof. D. J. L. Brett, Prof. P. R. Shearing
Electrochemical Innovation Lab
Department of Chemical Engineering
UCL
London WC1E 7JE, UK
E-mail: p.shearing@ucl.ac.uk

 The ORCID identification number(s) for the author(s) of this article can be found under <https://doi.org/10.1002/aenm.202002655>.

© 2020 The Authors. Advanced Energy Materials published by Wiley-VCH GmbH. This is an open access article under the terms of the Creative Commons Attribution License, which permits use, distribution and reproduction in any medium, provided the original work is properly cited.

DOI: 10.1002/aenm.202002655

Dr. T. M. M. Heenan, A. Wade, Dr. C. Tan, Dr. D. Matras, Dr. A. S. Leach, Dr. J. B. Robinson, A. Llewellyn, A. Dimitrijevic, Dr. R. Jervis, Dr. P. D. Quinn, Prof. D. J. L. Brett, Prof. P. R. Shearing
The Faraday Institution
Quad One
Harwell Science and Innovation Campus
Didcot OX11 0RA, UK
Dr. J. E. Parker, Dr. D. Matras, Dr. P. D. Quinn
Diamond Light Source
Harwell Science and Innovation Campus
Didcot OX11 0DE, UK

produce Ni oxides; whereas the latter yields insufficient capacity for many applications and capacity fading issues arising due to Mn dissolution. The combination of both Ni and Mn to produce $\text{LiNi}_x\text{Mn}_y\text{O}_2$ ^[6] improves upon these issues but can still suffer significant capacity fade due to Li/Ni disordering (also known as “crystallographic disordering”). Promising results have been demonstrated through the combination of the three elements to produce $\text{LiNi}_x\text{Mn}_y\text{Co}_z\text{O}_2$ (NMC), which offers theoretical capacities on the order of 270 mAh g⁻¹, although disordering can also be problematic in NMC.^[7] Additionally, the sourcing and disposal issues associated with Co favor Ni-rich variations of the NMC, for example, where $x > 0.5$.^[8] Specifically, NMC811 (where $x \approx 0.8$) can produce high reversible capacities (>200 mAh g_{NMC}⁻¹) and favorable rate capabilities (electronic conductivity $\approx 2.8 \times 10^{-5}$ S cm⁻¹ and Li⁺ diffusivity of 10⁻⁸ to 10⁻⁹ cm² s⁻¹), making it one of the most promising candidates for the next-generation of cathodes within BEVs. Several comprehensive reviews of cathode developments can be found by Nitta et al., Andre et al., and Mohanty et al.^[1,9,10] The higher Ni-content within NMC811 allows for a greater specific energy at a lower cell potential; for instance, at 4.2 V (vs graphite), NMC111 can achieve ≈ 500 Wh kg⁻¹, whereas NMC811 can achieve >600 Wh kg⁻¹ (with respect to the mass of active material). However, high Ni content NMC is more prone to oxygen release through the chemical and electrochemical oxidation of the electrolyte. This occurs at lower cell potentials of around 4.2 V (vs graphite) for NMC811 but does not occur until ≈ 4.6 V for both NMC111 and 622.^[11] Therefore, in order to extend the drivable range of BEVs that employ NMC811 as the cathode material, we must understand high-voltage degradation mechanisms in order to increase the practical upper cut-off potentials and achieve greater specific energies.

The relationship between the electrode crystallography, microstructure, and the electrochemical performance is well known and spans many length scales. For instance, it has been reported that through operational cycling, oxide materials may be susceptible to lattice-invariant shearing, resulting in irreversible structural changes.^[12] Additionally, the release of transition metals via dissolution^[13] as well as surface restructuring through the formation of other crystallographic phases^[14,15] remains problematic. To understand structural issues further, X-ray techniques have proven highly useful in the characterization of NMC electrodes. Particularly for high voltage cycling of NMC111, X-ray diffraction computed tomography (XRD-CT) has exposed heterogeneities in 3D^[16] and single particle nano-CT has revealed individual secondary particle cracking.^[17] As interest has moved toward Ni-rich NMC, it has recently been reported that the rapid analysis of raw powders can be capable of resolving defects before operation in NMC622 and NMC811^[18] although minimal particle cracking was observed at this stage in the particles' lifetimes (i.e., before printing into electrode sheets). At the atomic scale, it is thought that the Ni–Li anti-site defects formed during operation may be a precursor for inter-granular cracking within NMC811,^[19] and because each primary particle is expected to be a single crystal, or grain, this is also often described as the dislocation of primary particles, that is, the cracking and separation of primary particles. Moreover, when an NMC811 electrode is de-lithiated, the interlayer spacing gradually increases with the cell's state of charge (SoC),

before collapsing at high SoC; this is also thought to induce further strain between primary particles within the secondary particle agglomerates.^[20]

In conclusion, the literature reports a myriad of mechanisms that may act as precursors for operational particle cracking in NMC^[21] and although promising efforts are being made to pursue new materials to combat these issues,^[22] further knowledge is required of cracking within NMC811 cathodes. Firstly, minimal cracking is anticipated in raw powders^[18] but after operation, many particles are expected to possess defects, accompanied by a loss of electrochemical capacity. Therefore in this work we begin by examining a pristine electrode before operation to quantify the pre-existing particle defects that have originated from the electrode sheet manufacturing processes. We then explore the macrostructure of electrodes operated to various upper cut-off potentials to study the relationship between bulk mechanical integrity and cell potential. Building upon this, we investigate the defect severity in the secondary particles at a higher magnification outlining possible methods for detecting and quantifying such defects with statistical confidence. To compare the defect severity to the degree of crystal and chemical disorder, we then study several individual secondary particles in considerable detail. And finally, we quantify primary particle interactions and degradation with the highest possible zone-plate X-ray imaging resolutions. Overall this work begins at the macroscopic length scale of the electrode sheets and works through each of the subsequent major length scales down to the crystal structure, inspecting the various forms of defect formation due to high voltage operation at each respective stage. To do so, here we employ a range of X-ray characterization methods including: lab-based micro- and nano-computed tomography (CT), with complementary synchrotron X-ray diffraction (XRD) and fluorescence (XRF). We focus specifically on the first observations of cracking and also outline the methodology for the exploration of long-duration analysis that may form the basis of future work to extend cell lifetimes.

2. Results

2.1. Defects Due to Fabrication

Electrode sheets can be fabricated in various ways. For instance, the amount of active material, coating method (e.g., single- or double-layer) and the calendaring pressure can all be tuned to suit the application. Due to the range of manufacturing parameters that affect the electrode design, the electrode material that is examined throughout this article (“Material 1”) has also been compared to a commercial electrode with contrasting features (thickness, loading, etc.) to provide a comprehensive assessment of defects induced during fabrication. This comparison can be found in detail within the Supporting Information. **Figure 1** reports the X-ray nano-CT analysis and defect assessment. The electrode sample was taken from a thin (≈ 30 – 40 μm) single-layer sheet with a low areal capacity (≈ 2 mAh cm⁻²). Unlike previous reports of the potential defects that may be visible in raw powders which consist predominantly of internal voids or variations in surface roughness,^[18] a significant proportion of the particles in the printed electrode possessed some

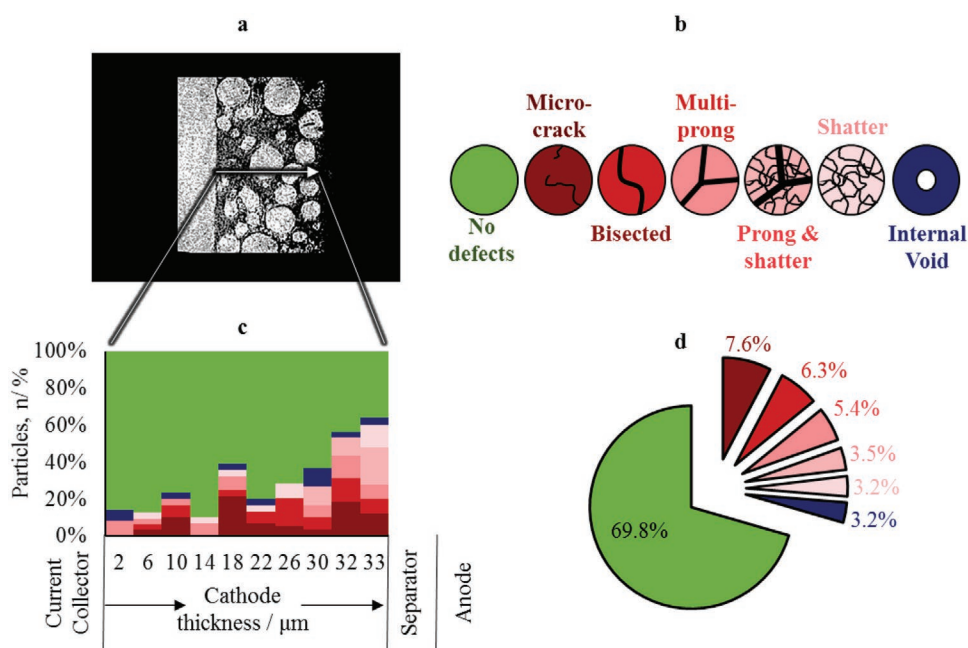


Figure 1. Quantifying the number of defective particles within pristine (pre-operated) NMC811 electrode structures through the definition of several defect categories: a) grayscale ortho-slice image taken from the 3D tomogram; b) a visual aid of the seven categories of particle defect proposed here; c) the percentage population of each defect with respect to the distance from the current collector; and d) the average particle defect composition. The comparison to the commercial standard can be found within the Supporting Information.

form of cracking defect, even before operation (Figures S1 and S2, Supporting Information).

In order to quantify these defects, the authors have defined several particle categories; this is not intended as an exhaustive list as more defects may be discovered in future work and the authors encourage readers to expand this list by developing methods that allow for the discovery of other categories. The categories defined here are summarized in Table 1 and visualized in Figure 1. The 3D datasets for Material 1 and the commercial comparison were then explored starting at the electrode–current collector interface and working to the electrode–separator interface, counting the number of particles of each category along the electrode thickness. As with all CT imaging techniques, there is a trade-off between resolution and statistical representation. In this work, a large number of particles were assessed (158 particles) in order to generate the quantitative analysis displayed within Table 1 and several hundred more were assessed within the second material (401 particles from a commercial source) that is reported within the Supporting Information (See Figures S1–S3,

Supporting Information, for raw data and comparisons between the two materials).

Before exploring the spatial variations with respect to electrode thickness, it is useful to assess the electrodes as a whole. Notably, an order of magnitude fewer particles display internal void structures within the commercial material, compared to Material 1. As mentioned previously, internal voids have been observed in raw powders before the production of coatings and have therefore been attributed to secondary particle manufacturing, rather than printing or calendaring.^[18] They do, however, pose the substantial drawback of wasted volume, and thus may be detrimental to volumetric energy and power densities, although there have also been reports of the potential mechanical benefits of such structures, where the electrochemical expansion/contraction stress during (de)lithiation mechanisms can be relieved.^[23] There are approximately 4% more defective particles in the commercial material—this disparity may be because the commercial material displayed a greater amount of cracking for almost all categories, which we hypothesize to

Table 1. Particle categories for pristine defect quantifications within printed NMC811 cathode sheets.

Category	Description	Material 1 [%]	Commercial comparison [%]
No defect	No obvious defects are visible	69.8	65.8
Internal void	An isolated void is located below the particle surface	3.2	0.2
Micro-crack	Small crack(s) that do not span the entire particle diameter	7.6	9.2
Bisect	A single large crack that splits the particle in two	6.3	7.0
Multi-prong	Two or more large cracks that split the particle into multiple sections	5.4	8.2
Prong & shatter	One or more large cracks that split the particle but with additional micro-cracks	3.5	2.5
Shatter	The particle has split into many small fragments (the size of primary particles) via multiple cracks	3.2	7.0

be due to the calendaring requirements of such a thick, high-loading electrode. Although the exact calendaring parameters are not known to the authors, the likelihood of particles stacking and forming localized stress peaks would be higher for a higher loading electrode. Particularly, the commercial material displays more than double the number of shattered particles and far more particles that have two or more large cracks (multi-prong). Moreover, several particles have been pressed into the current collector, suggesting that (at least locally) the calendaring pressure was high enough to exceed the yield point of Al and plastically deform the dense metal current collector sheet.

Finally, the degree of cracking was assessed with respect to the electrode thickness, revealing that both Material 1 and the commercial comparison exhibit more cracking toward the electrode-separator interface. This is most likely to be the surface in contact with the calendaring instrument during fabrication. For instance, over 50% of particles exhibit defects at the electrode-separator interface, for both materials. The degree of cracking is observed to decline away from the surface and then peak again toward the center of the electrode, before again declining toward the current collector. The fact that this is observed in both samples indicates that the mechanism responsible for these defects is not unique to single- or double-layer electrodes, nor low- or high-loadings. 4D studies such as the work by Daemi et al.^[16] can aid in our understanding of these manufacturing defects. For instance, is a certain critical calendaring pressure or electrode loading required in order to deteriorate a micro-crack into a shattered particle? Can we achieve similar areal loadings without surpassing this point? Future work may explore this, but the results displayed here outline that substantial cracking of around one third of particles could be present before routine operation even begins for NMC811 cells.

2.2. Electrode Level Defects Due To Early-Stage Cycling

Operating to high voltages induces irreversible degradation^[10] but would allow access to higher capacities; consequently, understanding high-voltage degradation is of significant interest. To examine the influence of electrochemical cell potential during early-stage cycling upon the production of operationally-induced cracks, several coin cells were fabricated from the same batch as Sample 1. To emulate as close to real-world application as possible, the NMC811 cathodes were cycled against graphite anodes (rather than Li metal) for five operational cycles after formation, then disassembled at low voltage (3.0 V) for X-ray CT imaging. The microstructures are displayed in Figure 2 for each upper cut-off cell potential (4.2–4.5 V).

At the electrode-level (imaged to produce a 1.57 μm reconstructed isotropic voxel length), the samples cycled to higher cut-off voltages (4.4 and 4.5 V) displayed delamination from the current collector and macroscopic cracking throughout the electrode sheet (i.e., throughout the active material and carbon-binder-domain (CBD) coating), this can be seen in Figure S4, Supporting Information. However, these features were attributed to the sample preparation; when the cells were disassembled, the electrode coating and current collector remained attached through visual inspection but micro-delamination may have already been present. As discussed in the methods

section, to prepare the samples for CT imaging, 1 mm diameter disks were punched from the 10 mm diameter electrode sheets. This is a standard procedure for large sample preparation, but when doing so, the majority of the high upper cut-off voltage samples detached from the current collector, whereas low voltage samples did not. This suggested that the mechanical integrity was already compromised for the high-voltage samples and is potentially a binder issue, rather than just active material cracking. This could have implications for kinks in the windings of cylindrical cells or the fold edges of prismatic cells, where the materials are under high stress.^[24] Highly elastic binders have been proposed previously to improve the cyclability of such cells showing great promise.^[22] Moreover, the effects of novel binders upon the delamination and macro-scale cracking of the coating could be studied in future work for Ni-rich NMC taken to high potentials within various geometries such as cylindrical, prismatic, and pouch.

At the particle-level (imaged to produce a 200 nm reconstructed isotropic voxel length), there are no signs of substantial surface degradation apart from a possible reduction in surface roughness (Figure 2b). Although, sub-surface features varied considerably; the grayscale at the core dropped substantially for many high-voltage particles, whereas this was not observed for low-voltage particles. To explore whether structural defects may be causing these grayscale variations, two particles were chosen from the high-resolution images displayed within Figure 1: one defective and one pristine, these are displayed within Figure 2d.

To emulate imaging these particles at various resolutions, for example, using a nano- and micro-CT instruments, the high-resolution data was binned, artificially increasing the voxel length, and decreasing the imaging spatial resolution. A line scan was then drawn across the low- and high-resolution images in the same location to compare the grayscale variation across the sample. Figure 2d demonstrates that although the partial averaging (induced through the use of lower resolutions) smooths the variations across the particles, particles with defects (red) still display a far greater grayscale variance compared to particles without defects (blue). This finding is highly useful—one of the major drawbacks of high-resolution imaging is the lack of material statistics, however, if one can use grayscale variations as a proxy for degradation, a significantly larger number of particles can be examined by reducing the spatial resolution during acquisition. Lower resolution imaging that is capable of capturing many hundreds of particles in a single scan can be used to quantify the number of defective particles even if the fine detail of the defects is indistinguishable. Moreover, the defects described in Figure 1 may produce grayscale variations with specific functions which can be determined if enough data can be assessed, that is, thousands or tens of thousands of individual particles. The authors envisage that future work could look to collate very large data libraries of 3D cathode structures and subsequently analyze the intra-secondary-particle grayscale variation for every particle, for example, potentially thousands of particles per tomogram providing thousands of data points per electrochemical history. Moreover, due to the potential for a very high number of data points, this methodology would lend itself well to intelligent computation such as machine learning which may form another avenue of future work.

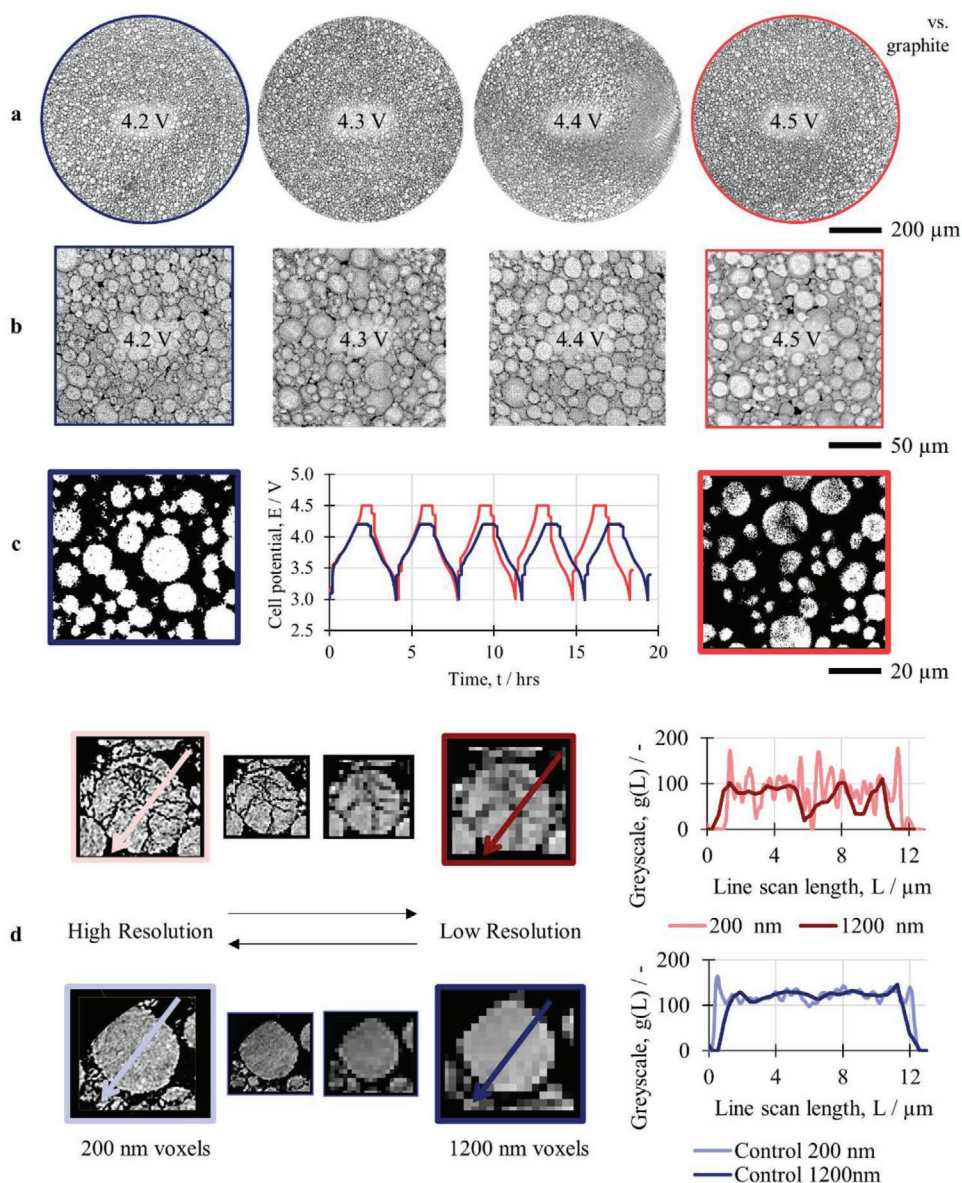


Figure 2. Using X-ray-CT to assess electrode- and particle-level degradation in NMC811 cathodes taken to various upper cut-off voltages: a) 3D grayscale volume renders at the electrode-level (1.57 μm isotropic voxel length); b) 3D grayscale volume renders at the particle-level (206 nm isotropic voxel length); and c) 2D grayscale ortho-slices taken from the 4.2 and 4.5 V structures with the same grayscale threshold applied to display grayscale variations; accompanied by the electrochemical cell potential plotted with respect to time; d) two examples of a defective (red) and pristine (blue) particle and their intra-particle grayscale variation with respect to imaging resolution.

2.3. Particle Level Defects Due To Early-Stage High-Voltage Cycling

In order to further investigate secondary particles operated to high-voltage, several particles were extracted from the electrode that had been cycled to 4.5 V (red in Figure 2a). These particles were re-mounted without the accompanying bulk material to be characterized with improved signal-to-noise. First, the particles were imaged in 3D using a lab-based X-ray nano-CT with zone-plate focusing optics, and second, they were inspected via combined X-ray diffraction with fluorescence characterization using a synchrotron nanoprobe beam.

Figure 3 displays the printed electrode tomogram (as previously seen in Figure 2a) alongside seven individual particles removed from this sample. The lab-based X-ray CT imaging allowed the grayscale histogram to be calculated for each individual particle (Figure 3b,c), along with the intra-secondary-particle grayscale variation with respect to radial position (Figure 3d) and the particle equivalent diameters (Figure 3e). As mentioned previously, increased partial averaging (a shift of the histogram grayscale peak to darker colors or lower numbers) is an indication of greater intra-particle void-space and thus, potentially an increased population of defects such as cracking. These particles were all imaged within the same tomography scan and

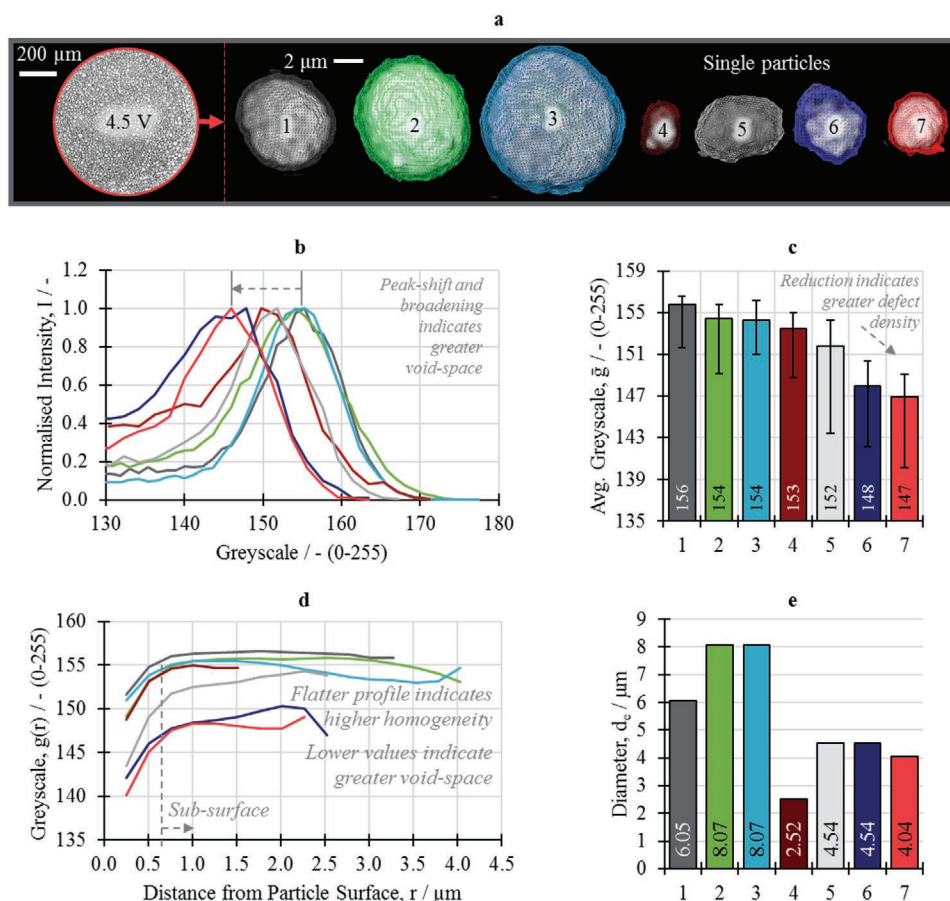


Figure 3. Analyzing single NMC811 particles that have been cycled to high voltages using X-ray CT: a) seven particles analyzed individually all harvested from the same printed electrode sheet; b) the grayscale histogram of each individual particle; c) average grayscale value for each particle where error bars indicate the max and min grayscale within the particle; d) grayscale value with respect to the distance from the particle surface; e) each particle's equivalent diameter.

detected within the same tomogram. As such, artefacts such as incident beam energy fluctuations can be considered negligible and each particle's grayscale values may be compared directly. Within Figure 3, the particles have been ordered according to their average grayscale value, whereby Particle 1 has the highest grayscale value and is therefore expected to contain the least microstructural defects, whereas Particle 7 has the lowest grayscale value, thus most likely contains the greatest population of defects. Figure 3d supports this with corroboration of the resolution dependency study in Figure 2d; particles with lower average grayscale values (greater partial average) exhibit less stable intra-secondary-particle grayscale variation beneath the particle surface. There does not appear to be a clear correlation between particle size and the defect severity. Therefore, at low C-rates (0.5C), particle sizes may not be of significant importance for secondary particle cracking. To examine the same particles further, they were then transported to the I14 nanoprobe beamline at Diamond Light Source for continued analysis.

Figure 4 displays the results from the synchrotron nanoprobe XRF and XRD measurements. Within the figure, the particles are ordered as within Figure 3. There are several key observations from this data. Firstly, the inter- and intra-secondary particle Mn content varies considerably. This suggests that Mn

dissolution may be important during the early stages of cycling (e.g., 1–5 cycles). It can also be seen that the average particle has a Ni:Mn:Co ratio of $\approx 83:7:9$ instead of 80:10:10. Moving to the XRD analysis, neither the r_1 -factor, the ratio of the c and a lattice parameters, nor the I_{003}/I_{104} ratio appear to correlate with the degree of cracking. This could be influenced by the diffraction statistics; there will always be fewer diffraction interactions when examining a single particle compared to bulk powder diffraction, making direct comparisons of diffraction intensities less reliable, although, approximately 40 000 patterns were collected for each particle and then summed before refinement and analysis. Moreover, this material contains hundreds of primary particles arranged randomly within each secondary particle structure and thus, a significant number of crystals could still be analyzed. Also reported are the H2/H3 and rock salt diffraction intensities; however, relative to the NMC, these structures appeared in very low quantities and should therefore be considered qualitative.

When examining the XRF data from Particle 2, it became clear that an unknown material, very rich in Mn was present on Particle 2's surface, existing not as a coating, but resembled an external cluster on the surface of the secondary NMC particle (Figure 5). Without 4D studies (three spatial dimensions plus time), we cannot definitely confirm whether this is a defective

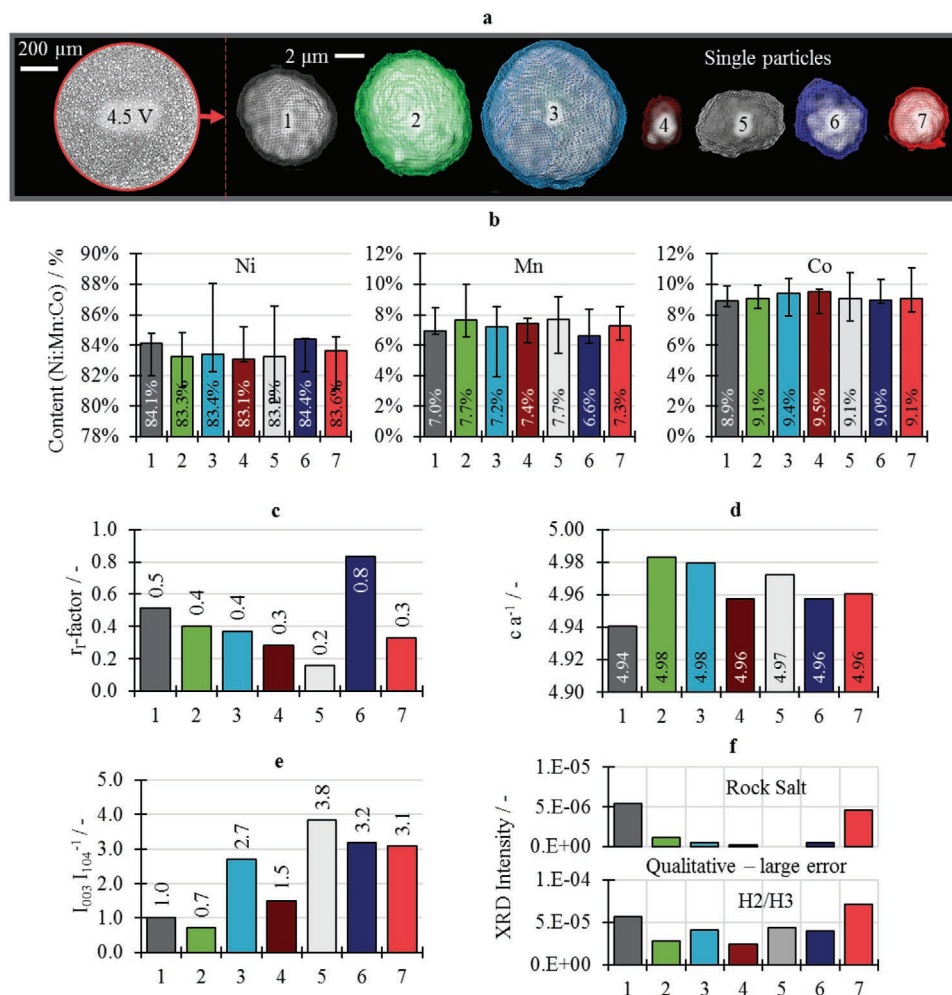


Figure 4. Analyzing single NMC811 particles that have been cycled to high voltages using XRD and XRF: a) Seven particles analyzed individually all harvested from the same printed electrode sheet; b) Ni, Mn, and Co content calculated from the XRF spectra; and c) r_1 -factor; d) ratio of the c and a lattice parameters; e) ratio of the 003 and 104 reflection intensities; f) intensities for the rock-salt and H2/H3 phases, all calculated from XRD measurements.

“cluster” formed during fabrication/manufacturing processes as a contaminant or formed as a by-product of high-voltage operation. Regardless of origin, this structure is undesirable and has potential implications upon cell operation. The structure may be unstable and could breakdown or grow during operation, having potential implications upon the intercalation mechanisms and side reactions; however, the structure may also be electrochemically and chemically stable but still poses the issue of increased tortuosity for Li^+ transport within the electrolyte (ions must travel around the Mn cluster to reach active material) and wasted volume that the cluster consumes (i.e., that could be filled with useful active material). It is therefore of considerable interest to study such a cluster, regardless of origin.

Figure 5 outlines this cluster in more detail with comparison to several other features of interest; at the NMC particle core, surface and a lone primary NMC particle on the secondary particle surface. Here, subsurface information was obtained using XRF-CT, unlike all data presented in Figure 4 that was collected using 2D XRF mapping and averaged for the whole particle. It was found that the Mn content increased toward the particle surface and displayed small peaks either side of a micro-crack

where the local Mn content (in the ratio Ni:Mn:Co) climbs from ≈ 4 to 6%. Moreover, the Mn-rich cluster on the secondary NMC particle surface is significantly less attenuating than the NMC, suggesting it is likely far less dense. Along with the considerable inter- and intra-particle Mn content variation that was observed in Figure 4b, this suggests that the Mn is not stable during early stage cycling. This is important because the Mn is thought to stabilize the Ni through the donation of an electron that reduces the Jahn–Teller distortion and then remains electrochemically inactive throughout the cell operating potential range.^[25] If the Mn is leaving the structure, or is mobile enough to trigger intra-particle heterogeneities, then the Ni may become unstable triggering greater crystal disorder. To examine this, the particles were analyzed further, excluding the Mn rich particle; this is presented in Figure 6. Within the figure, the remaining six particles are examined with the Mn content for that particle. It can be seen that the c lattice parameter increases as the minimum Mn content declines; moreover the r_1 -factor increases as the average Mn content decreases. These are examined with a linear fitting that shows relatively small deviation ($R^2 = 0.9$ and 1.0 to 1 d.p., respectively). To conclude, the Mn

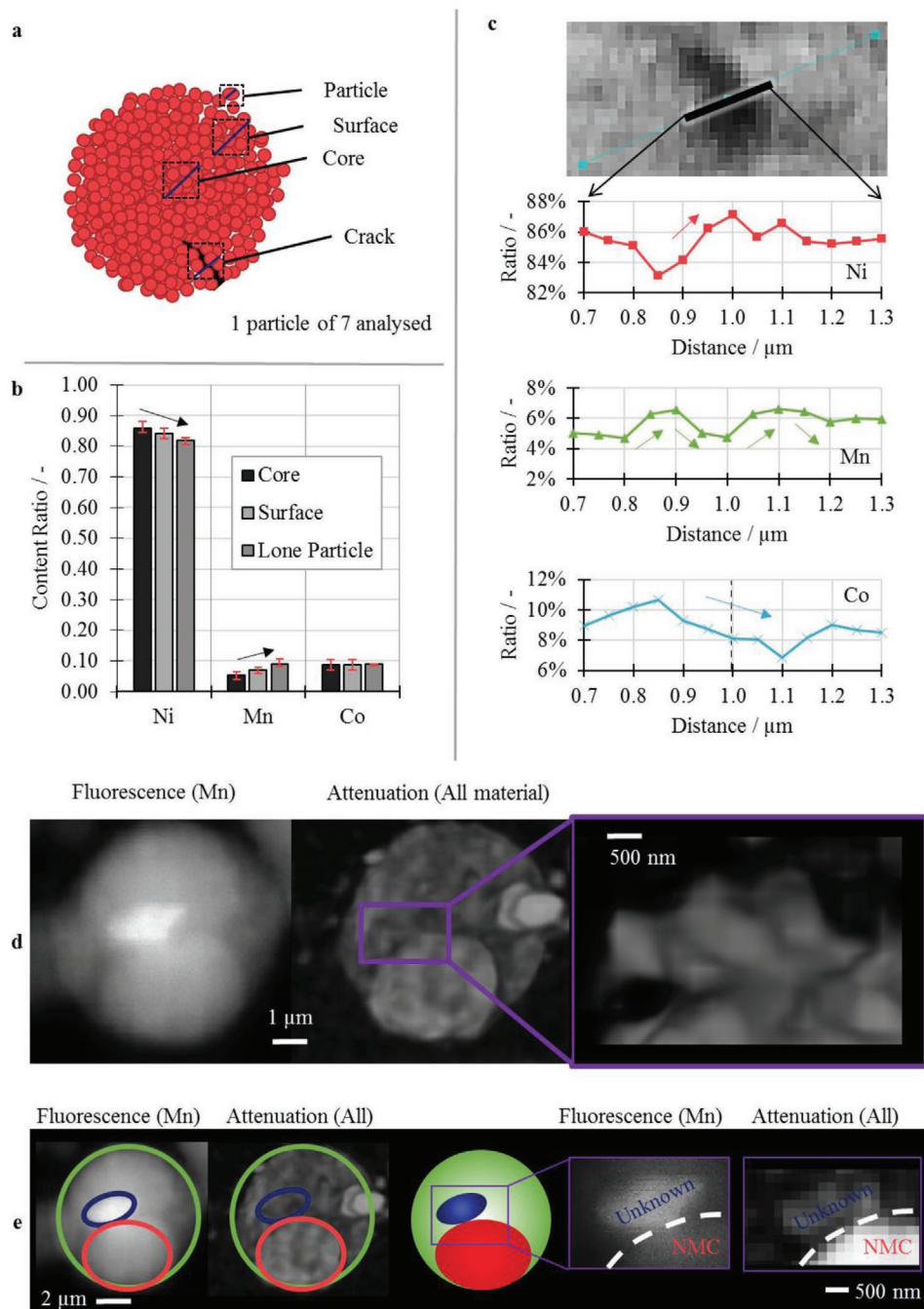


Figure 5. Examining non-uniform Mn content within a secondary NMC811 particle: a) a schematic illustration as a visual aid for the four features of interest; b) the content of Ni, Mn, and Co for the core, surface and lone surface particle; c) the content through an internal crack; d) a Mn fluorescence and all material attenuation map, with the Mn-rich cluster magnified; e) separation of the Mn-rich cluster and comparison of the fluorescence and attenuation data.

may be particularly mobile during low cycle numbers, resulting in inter- and intra-particle heterogeneities and ultimately Mn dissolution, and the crystal structure appears to be influenced by the Mn content. Although, neither the Mn content nor the crystal disordering correlate with the secondary particle cracking for low C-rates (0.5C) early stage cycling (1–5 cycles).

From the X-ray CT, XRD, and XRF data, we have concluded that from the particles studied, there appears to be a disconnect

during early stage cycling between the defects associated with secondary particle cracking and the crystal–chemical dynamics. Although the Mn content appears to affect the crystal stability, this does not translate to secondary particle cracking, at least for low cycle numbers. Secondary particle cracking has been reported previously for lower Ni content NMC particles,^[17] therefore it is of interest to see if the cracking experienced by low and high Ni content NMC appears similar in structure. To

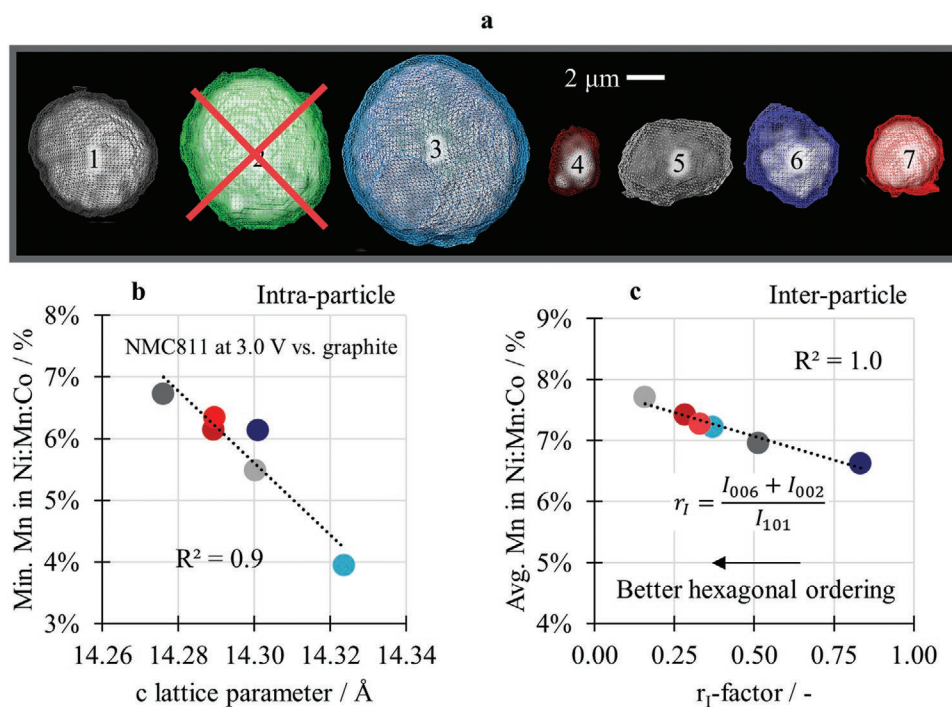


Figure 6. Analyzing single NMC811 particles using XRD and XRF that have been cycled to high voltages: a) seven particles analyzed individually, all harvested from the same printed electrode sheet with one particle (number 2) omitted from analysis due to the presence of a heterogeneous Mn-rich cluster; b) the minimum Mn content plotted with respect to the c-lattice parameter for each particle; and c) the r_1 -factor plotted with respect to the average Mn content for each particle. Particle microstructures were produced from nano-CT; Mn content was determined from XRF data and the c-lattice parameter and r_1 -factors were calculated from the XRD data.

examine the cracking in greater detail, we repeated the nano-CT at the highest available spatial resolution.

Figure 7 shows the investigation of two secondary particles of similar size ($\approx 16\text{--}18\ \mu\text{m}$ diameter). These are different particles to those displayed within Figures 1–6 but they are all from the same batch of Material 1. One particle had undergone no operational cycling and was imaged in the pristine state (green), the other had been cycled to an upper cut-off voltage of 4.5 V for five cycles before disassembly at 3.0 V for imaging (red). When viewing the 3D surfaces at high resolution there is not a great difference between the two secondary particles. However, the subsurface features were resolved well and significant difference in features could be easily distinguished. There are two 2D ortho-slices displayed within Figure 7a,b which highlight these disparities.

The first substantial observation is that neither structure is fully dense. The pristine structure contains many void-spaces between the primary particles, some of which may be isolated from the surface. Several channels are visible that span up to $\approx 2\ \mu\text{m}$ in length from the particle surface alongside larger heterogeneous pores within the structure that span $\approx 500\text{--}900\ \text{nm}$. These features are illustrated by the skeletal map of the void structure within Figure 7a.

The high-voltage particle displays similar features, that is, voids and channels, but substantially worsened due to operation. The channels penetrate far further in the operated particle, with lengths of up to $8\ \mu\text{m}$. The void skeleton highlights this as well as displaying localized clusters of more severe degradation. Figure 7c quantifies these void-structures with respect to the distance from the secondary particle surface. The pristine structure

is relatively homogenous, with a local void fraction that is generally independent of the radial location; whereas the operated particle experiences a great void percentage toward the particle core. This can be explained by the fact that the cracks converge toward the central core; crack density increases with distance from the secondary particle surface. The presence of cracks also results in a general higher void fraction, as seen in Figure 7d.

Many primary particles within the pristine secondary particle microstructure were either too close to distinguish a boundary or were fused together during fabrication. Therefore, when quantifying the primary particle size distribution (PSD), two “fused” particles were considered as one, because accurately defining their boundary was not possible at this resolution. For the boundaries that were detectable, the primary particles were segmented and analyzed individually to produce a PSD (based on primary particles), as seen in Figure 7e. The same was done for the operated sample, however it was noticed that there were far fewer “fused” particles within the operated sample. Therefore, the calculation of a PSD would provide an indication of the proportion of separation after cycling, that is, how many “fused” particles became detached. An example of a pair of fused particles from the pristine structure is displayed within Figure 7f. The average measurable primary particle diameter decreases after operation, likely due to the separation of what were previously “fused” or highly tightly packed primary particles. The reduction is quite substantial with the average measurable diameter reducing from $\approx 1\ \mu\text{m}$ to $600\ \text{nm}$, suggesting a large proportion of the primary particles have been displaced and disconnected. It should be noted that we were able to

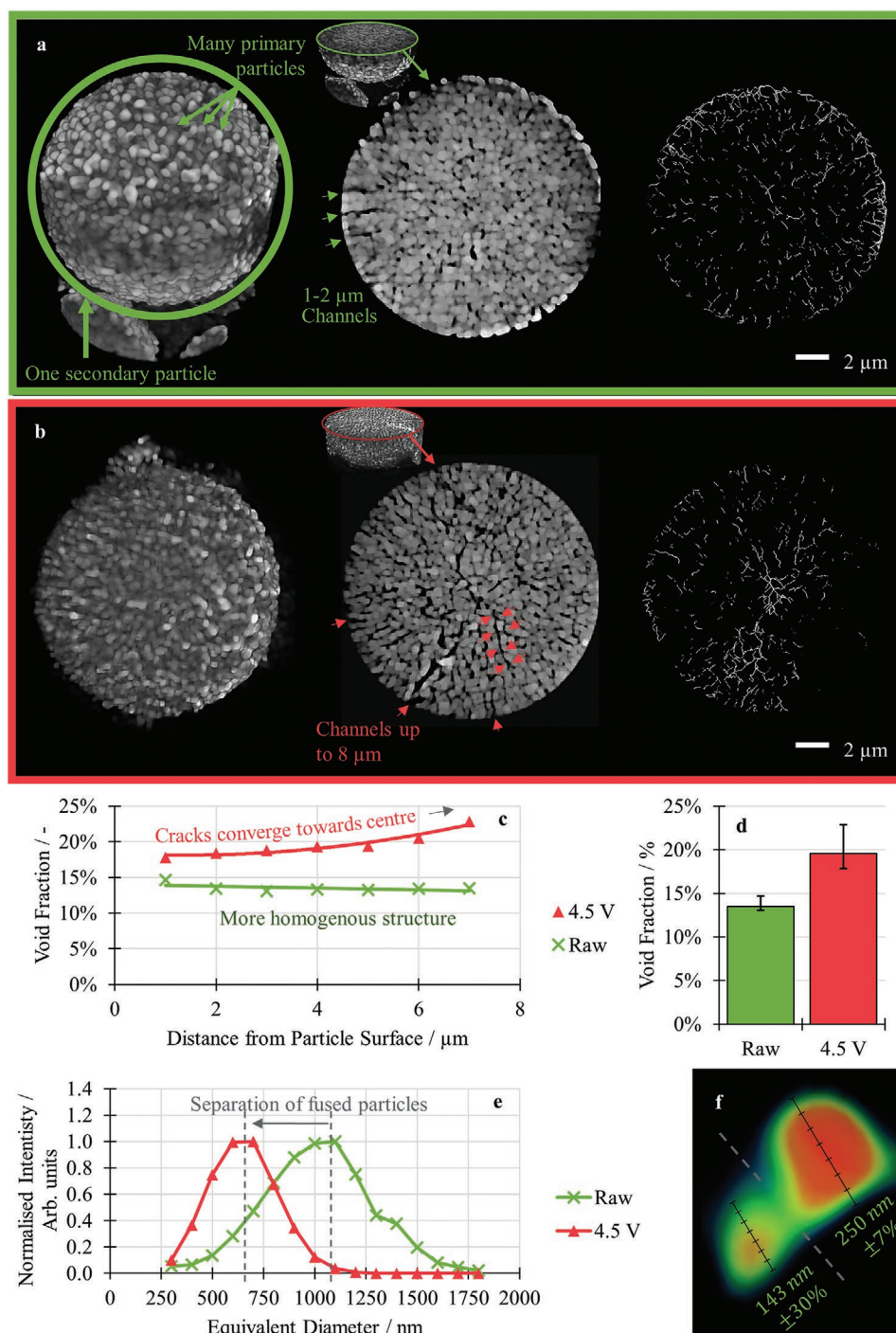


Figure 7. Studying NMC811 primary and secondary particle microstructures at the spatial resolution limits of zone-plate X-ray imaging: A 3D volume render, 2D ortho-slice and pore skeleton map for a) a pristine secondary particle with no cycling, and b) an aged secondary particle charged to 4.5 V versus graphite five times then discharged to 3.0 V versus graphite before disassembly and imaging; c) the void fraction between primary particles as a function of depth from the secondary particle surface; d) the average void fraction with error bars indicating the maximum and minimum values for each particle; e) equivalent particle diameters for the constituent primary particles; and f) magnification of two potentially “fused” primary particles from the pristine secondary particle.

assess many primary particles in this analysis (Figure 7) producing a good statistical representation of the primary particles within these two secondary particles, however, in order to determine whether these two secondary particles are representative of the bulk material ideally there should be tens or even

hundreds of secondary particles (i.e., thousands of primary particles) assessed. Maintaining this high resolution while also characterizing many secondary particles is unrealistic with the current imaging capabilities but may be possible as higher brilliance X-ray sources are developed.

It should be noted that, as with all image-based characterization methods, the spatial resolution can dictate the precision of the quantification. Consequently, there are features that are not observable here, even when using some of the highest resolution currently possible with lab-based X-ray microscopes. For instance, there may be nano-particles that occupy what appears to be void-space at this resolution, artificially increasing the void-fraction. However, the quantification methods were identical for the two particles, therefore we can place high confidence in their comparison and relative changes observed on cycling.

These studies may be extended to further the precision of the quantification through non-lab-based methods. For example, imaging that is wavelength limited (e.g., coherent diffraction imaging, CDI) can allow for individual crystals to be characterized, that is, crystals within the primary particles. Future work may look to explore the impact of high-voltages to understand the dynamics beyond the primary particle-scale. Another aspect to consider is that the crystal domains are not aligned within a polycrystalline particle. As mentioned previously, these are polycrystalline materials whereby the secondary particle is composed of many hundreds of primary particles that are randomly orientated. Previous work has also explored the role of primary particle alignment within the secondary particle agglomerates and the potential impacts upon charge distribution,^[26] and various methods are emerging to combat this including single crystal alternatives.^[27] The various orientations of the grains may dominate the stress and crack formation during operation which would explain the similarities in NMC811 and NMC111 cracking structures. Recent work has demonstrated the importance of grain orientation^[28] and speculated on their implications. Whereas the Mn instability and general lack of Mn to stabilize the Ni within Ni-rich chemistries may accelerate the capacity fade at the primary particle scale.^[29] Naturally, greater cracking densities increase the chance of surface restructuring to other crystalline phases (e.g., rock-salt), thus cracking will lead to capacity fade too but their contributions may be distinct.

3. Conclusion

Although NMC811 is a popular choice for the next-generation of automotive lithium-ion batteries, complex degradation mechanisms continue to impede performance during application. In this work, we employ a variety of X-ray characterization methods using both lab and synchrotron sources to explore such mechanisms and their relationships.

We show that although cracking may be minimal after secondary particle fabrication, once the active material is printed into a sheet and calendared, the fabrication-induced cracking can be severe, with approximately one-third of particles being defective before operation. Moreover, these defects become more severe near the cathode–separator interface, a trend that was seen in two very different electrodes suggesting that this may be true for single- and double-layer fabrication designs, as well as high and low-loading electrode sheets.

Macroscopic degradation in the form of delamination and the loss of bulk mechanical integrity may be experienced after

high voltage operation which is thought to be linked to binder adhesion degradation; future work may explore this in more detail. This would be most significant for kinks within cylindrical windings or prismatic cells, but may be overcome by the promising work emerging on highly elastic binders. Previous work has demonstrated that distinguishing between the CBD, the active material (NMC) and void-space via three-phase segmentation is challenging but not impossible.^[30] In addition to exploring the delamination of the electrode from the current collector, as has been done here, delamination of the CBD from the active material could be explored in future work. Moreover, by combining imaging from several X-ray interactions, for example, absorption, phase-shift, diffraction and fluorescence, could allow the conductive and binding carbon within the CBD to be distinguished, that is, four-phase segmentation, allowing further insight.

To develop high statistical confidence in the dynamics of particle cracking during operation, the sub-surface grayscale variations may be used as a proxy for detecting cracking defects within low-resolution X-ray tomograms and the application of this methodology may open avenues for new machine learning tools. This approach would allow defective and pristine particles to be distinguished, permitting the quantification of the population of defective particles within an electrode sheet using a relatively fast CT scan. For example, scan times on the order of 1–2 days would have previously been employed to detect defects and can now be replaced by scans of ≈ 2 h, while encompassing many hundreds of particles, producing significantly improved materials statistics.

When assessing individual particles at high resolution, it was found that particles of various diameters may all experience cracking and there does not appear to be a correlation between particle size and cracking severity for low C-rates and low cycle numbers. However, inter- and intra-particle Mn content (within the ratio of Ni:Mn:Co) varies considerably more than Co content after high-voltage cycling (4.5 V vs graphite). Small amounts of H2/H3 and rock-salt phases were detected even after low cycle numbers (five cycles). Moreover, the Mn content appears to be linked to the crystal ordering and may dominate transition metal dissolution during low cycle numbers. Finally, the voltage-induced cracking appears in Ni-rich chemistries (e.g., NMC811) in a very similar pattern to lower Ni content NMC (e.g., NMC111).^[31] It appears that the instability of the Mn within the NMC structure may be linked to the crystallographic disordering and can leave the NMC structure to form surface clusters; however when considering early stage cycling, this does not correlate clearly with the secondary particle cracking which may be dominated by processes during fabrication and the disconnection/separation of neighboring primary particles during electrochemical expansion/contraction.

Ultimately this work has highlighted several key findings with regards to particle defects and suggestions as to when and why they may form. We have demonstrated that manufacturing methods must be assessed in order to minimize fabrication-induced cracking, especially at the separator interface. Moreover, during high-voltage operation, macroscopic binder degradation may be significant, observed through the delamination of the electrode from the current collector and general loss of mechanical integrity. We have also shown that low-resolution

imaging can be used to detect defective particles with high sample throughputs, significantly improving materials statistics. Finally, the Mn mobility was seen to correlate with crystallographic degradation, impacting early stage (0–5 cycles) capacity loss; however, it does not appear to correlate with secondary particle cracking severity. Instead, secondary particles crack predominantly at the boundaries between primary particles and are thought to be dominated by electrochemical expansion and contraction during de/lithiation and therefore form cracking structures similar to lower content NMC (e.g., NMC111). This is thought to be exacerbated by the random grain orientations that are inherent in such polycrystalline materials. This study improves our knowledge of the sources and developments of defective particles, an improved understanding of which is essential in order to manufacture the high capacity and long-lasting cells which are urgently required for the commercialization of BEVs with extended drivable ranges and competitive lifetimes.

4. Experimental Section

Materials: All materials explored in this work were composed of an NMC811 as the active material (i.e., $\text{LiNi}_{0.8}\text{Mn}_{0.1}\text{Co}_{0.1}\text{O}_2$). The data displayed in Figure 1 originated from two sources: Material 1 was purchased as an electrode sheet from a commercial supplier (NEI Corporation, Summerset, USA), and Material 2 was purchased as a commercial LG Chem INR18650 MJ1 cell (NKON, Netherlands). Apart from Figure 1 where the two electrode types are compared, all other work was conducted on Material 1.

Electrochemical Cycling: Coin cells were assembled with NMC811 cathodes (Material 1) and graphite anodes from the same supplier (NEI Corporation, Summerset, USA). The electrodes were electrically isolated using a commercial separator material (CELGARD LLC, Charlotte, North Carolina, U.S.A.) and the cell was filled with a Li-ion electrolyte composed of 1 M LiPF₆ in EC:EMC (3:7). All of the coin cells were cycled using a Novonix battery cycler with integrated environmental chamber (NOVONIX Limited, Bedford, Canada) with a set point at 25 °C and all cells underwent the same formation step: a constant-current (CC) charge at C/20 followed by a constant voltage (CV) hold at 4.2 V (vs graphite) until the current dropped below C/40, then a CC discharge to 3.0 V at C/20. The operational cycling parameters varied between cells only in terms of upper cut-off voltage (which is stated throughout). All other parameters remained the same: they all followed a CC–CV protocol, at ≈25 °C, and were cycled with a CC charge C-rate of 0.5C (and C/20 CV cut-off) and discharge C-rate of 1C to a lower cut-off voltage of 3.0 V.

Laboratory Characterization: The X-ray imaging and data for Material 2 are reported elsewhere and publically available via a repository.^[32] Various samples were taken from Material 1 for imaging. All nano-CT data (Figures 1, 3–7) was conducted using an Ultra 810 X-ray instrument (Zeiss Xradia 810 Ultra, Carl Zeiss., CA, USA) employing a rotating chromium anode that produces a quasi-monochromatic beam with a characteristic emission peak at 5.4 keV (Cr–K α). Figures 1 and 3–6 report data with isotropic voxel lengths of 126 nm. Whereas Figure 7 reports data at a higher resolution with an isotropic 32 nm voxel length. All micro-CT data (Figure 2) was conducted using a Versa 520 X-ray instrument (Zeiss Xradia 520 Versa, Carl Zeiss., CA, USA) employing a stationary tungsten anode on a copper substrate that produces a polychromatic beam with a characteristic emission peak at 58 keV (W–K α). The micro-CT measurements were collected at two resolutions Figure 2a reports data with an isotropic voxel length of 1.6 μm and Figure 2b reports data with an isotropic voxel length of 0.2 μm . All reconstructions were achieved using commercial software using parallel- or cone-beam filtered-back-projection (FBP) algorithms: “Reconstructor Scout-and-Scan” (Carl Zeiss., CA, USA). Image quantification was

performed using commercial Avizo Fire software (Avizo, Thermo Fisher Scientific, Waltham, Massachusetts, USA.). In order to calculate the grayscale values for the individual particles displayed within Figures 3–6, spherical boundaries were defined that completely encapsulated the particles, then the pore and active material phases were segmented using standard grayscale cropping. This was all achieved in Avizo software. Then the binary dataset was compared to the raw grayscale data using Matlab (Mathworks, Natick, MA) to obtain a histogram exclusively for voxels that were defined to contain the active material (NMC). For the segmentation of the nano-CT data displayed within Figure 7, the raw grayscale data was processed using a non-local means filter and then segmented using a “bright” top-hat filtering segmentation, all completed using Avizo software.

Synchrotron Characterization: The particles displayed within Figures 3–6 were examined using Diamond Light Source I14 nanoprobe beamline using monochromatic beam of 19 keV. For each particle, the sample was rastered through stationary beam size of ≈50 nm through an area that entirely encompassed the particle. Diffraction and fluorescence data were collected simultaneously with 100 ms exposure time. Diffraction patterns were collected using an Excalibur 3M area detector, calibrated with a CeO₂ standard. Fluorescence spectra were collected using a RaySpec XRF SDD detector in the backscatter geometry with pulse processing and dead-time correction performed with the xspres3 system. Examples of the raw data can be found within the Supporting Information. The diffraction patterns were summed for the entire raster and the average 2D diffraction image was radially integrated using PyFAI software package.^[33] The analysis of diffraction data was performed with Topas 6 academic software.^[34] The fluorescence data was averaged for the whole particle with the integrated peak intensities of the three elements: Ni, Mn, and Co, used to determine the relative composition, that is, other elements may have been present but only the ratio of Ni:Mn:Co was of interest here. All XRF quantifications were based upon peak area ratios without correction for fluorescence cross-section or fluorescence yield differences. All XRF post-acquisition analysis was conducted in DAWN software (Diamond Light Source, Harwell).

Supporting Information

Supporting Information is available from the Wiley Online Library or from the author.

Acknowledgements

This work was carried out with funding from the Faraday Institution (faraday.ac.uk; EP/S003053/1), grant number FIRG001 and FIRG003; and the EPSRC grant EP/M014045/1. The authors acknowledge Diamond Light Source for time on beamline i14 under proposals sp20841 and mg23858. The authors would like to acknowledge the Royal Academy of Engineering (CiET1718\59) for financial support.

Conflict of Interest

The authors declare no conflict of interest.

Keywords

batteries, cathodes, degradation, electric vehicles, microstructure, NMC811, particle cracking

Received: August 17, 2020

Revised: October 1, 2020

Published online:

- [1] D. Andre, S. J. Kim, P. Lamp, S. F. Lux, F. Maglia, O. Paschos, B. Stiaszny, *J. Mater. Chem. A* **2015**, *3*, 6709.
- [2] K. Mizushima, P. C. Jones, P. J. Wiseman, J. B. Goodenough, *Mater. Res. Bull.* **1980**, *15*, 783.
- [3] A. Manthiram, *Nat. Commun.* **2020**, *11*, 1550.
- [4] T. Ohzuku, A. Ueda, M. Nagayama, *J. Electrochem. Soc.* **1993**, *140*, 1862.
- [5] R. Gummow, M. M. Thackeray, *J. Electrochem. Soc.* **1994**, *141*, 1178.
- [6] E. Rossen, C. D. W. Jones, J. R. Dahn, *Solid State Ionics* **1992**, *57*, 311.
- [7] E. Zhao, L. Fang, M. Chen, D. Chen, Q. Huang, Z. Hu, Q. B. Yan, M. Wu, X. Xiao, *J. Mater. Chem. A* **2017**, *5*, 1679.
- [8] C. B. L. Nkulu, L. Casas, V. Haufroid, T. De Putter, N. D. Saenen, T. Kayembe-Kitenge, P. M. Obadia, D. K. W. Mukoma, J. M. L. Ilunga, T. S. Nawrot, O. L. Numbi, *Nat. Sustain.* **2018**, *1*, 495.
- [9] N. Nitta, F. Wu, J. T. Lee, G. Yushin, *Mater. Today* **2015**, *18*, 252.
- [10] D. Mohanty, J. Li, S. C. Nagpure, D. L. Wood, C. Daniel, *MRS Energy & Sustainability* **2015**, *2*, E15.
- [11] R. Jung, M. Metzger, F. Maglia, C. Stinner, H. A. Gasteiger, *J. Electrochem. Soc.* **2017**, *164*, A1361.
- [12] M. D. Radin, J. Alvarado, Y. S. Meng, A. Van der Ven, *Nano Lett.* **2017**, *17*, 7789.
- [13] R. Jung, F. Linsenmann, R. Thomas, J. Wandt, S. Solchenbach, F. Maglia, C. Stinner, M. Tromp, H. A. Gasteiger, *J. Electrochem. Soc.* **2019**, *166*, A378.
- [14] F. Zhang, S. Lou, S. Li, Z. Yu, Q. Liu, A. Dai, C. Cao, M. F. Toney, M. Ge, X. Xiao, W. Lee, Y. Yao, J. Deng, T. Liu, Y. Tang, G. Yin, J. Lu, D. Su, J. Wang, *Nat. Commun.* **2020**, *11*, 3050.
- [15] F. Lin, I. M. Markus, D. Nordlund, T. C. Weng, M. D. Asta, H. L. Xin, M. M. Doeff, *Nat. Commun.* **2014**, *5*, 3529.
- [16] S. R. Daemi, C. Tan, A. Vamvakeros, T. M. Heenan, D. P. Finegan, M. Di Michiel, A. M. Beale, J. Cookson, E. Petrucco, J. S. Weaving, S. Jacques, *Phys. Chem. Chem. Phys.* **2020**, *22*, 17814.
- [17] P. C. Tsai, B. Wen, M. Wolfman, M. J. Choe, M. S. Pan, L. Su, K. Thornton, J. Cabana, Y. M. Chiang, *Energy Environ. Sci.* **2018**, *11*, 860.
- [18] T. M. Heenan, A. V. Llewellyn, A. S. Leach, M. D. Kok, C. Tan, R. Jervis, D. J. Brett, P. R. Shearing, *Adv. Sci.* **2020**, *7*, 2000362.
- [19] Q. Lin, W. Guan, J. Zhou, J. Meng, W. Huang, T. Chen, Q. Gao, X. Wei, Y. Zeng, J. Li, Z. Zhang, *Nano Energy* **2020**, *76*, 105021.
- [20] K. Märker, P. J. Reeves, C. Xu, K. J. Griffith, C. P. Grey, *Chem. Mater.* **2019**, *31*, 2545.
- [21] T. Li, X. Z. Yuan, L. Zhang, D. Song, K. Shi, C. Bock, *Electrochem. Energy Rev.* **2020**, *3*, 43.
- [22] B. Chang, J. Kim, Y. Cho, I. Hwang, M. S. Jung, K. Char, K. T. Lee, K. J. Kim, J. W. Choi, *Adv. Energy Mater.* **2020**, *10*, 2001069.
- [23] Y. Mao, X. Wang, S. Xia, K. Zhang, C. Wei, S. Bak, Z. Shadike, X. Liu, Y. Yang, R. Xu, P. Pianetta, *Adv. Funct. Mater.* **2019**, *29*, 1900247.
- [24] M. D. Kok, J. B. Robinson, J. S. Weaving, A. Jnawali, M. Pham, F. Iacoviello, D. J. Brett, P. R. Shearing, *Sustainable Energy Fuels* **2019**, *3*, 2972.
- [25] M. D. Radin, S. Hy, M. Sina, C. Fang, H. Liu, J. Vinckeviciute, M. Zhang, M. S. Whittingham, Y. S. Meng, A. Van der Ven, *Adv. Energy Mater.* **2017**, *7*, 1602888.
- [26] Z. Xu, Z. Jiang, C. Kuai, R. Xu, C. Qin, Y. Zhang, M. M. Rahman, C. Wei, D. Nordlund, C. J. Sun, X. Xiao, *Nat. Commun.* **2020**, *11*, 83.
- [27] W. Li, E. M. Erickson, A. Manthiram, *Nat. Energy* **2020**, *5*, 26.
- [28] A. Quinn, H. Moutinho, F. Usseglio-Viretta, A. Verma, K. Smith, M. Keyser, D. P. Finegan, *Cell Rep. Phys. Sci.* **2020**, *1*, 100137.
- [29] L. Yin, Z. Li, G. S. Mattei, J. Zheng, W. Zhao, F. Omenya, C. Fang, W. Li, J. Li, Q. Xie, E. M. Erickson, *Chem. Mater.* **2020**, *32*, 1002.
- [30] S. R. Daemi, C. Tan, T. Volkenandt, S. J. Cooper, A. Palacios-Padros, J. Cookson, D. J. Brett, P. R. Shearing, *ACS Appl. Energy Mater.* **2018**, *1*, 3702.
- [31] Z. Xu, M. M. Rahman, L. Mu, Y. Liu, F. Lin, *J. Mater. Chem. A* **2018**, *6*, 21859.
- [32] T. M. M. Heenan, A. Jnawali, M. Kok, T. G. Tranter, C. Tan, A. Dimitrijevic, R. Jervis, D. J. L. Brett, P. R. Shearing, *Data Brief* **2020**, *32*, 106033.
- [33] G. Ashiotis, A. Deschildre, Z. Nawaz, J. P. Wright, D. Karkoulis, F. E. Picca, J. Kieffer, *J. Appl. Crystallogr.* **2015**, *48*, 510.
- [34] A. A. Coelho, *J. Appl. Crystallogr.* **2018**, *51*, 210.